JGR Atmospheres

RESEARCH ARTICLE
10.1029/2022JD036565

Key Points:

- Frequently observed wind profile distortion (WPD) in the very stable boundary layer (VSBL) generates large turbulent eddies
- WPD-induced large eddies penetrate downward, leading to enhanced vertical mixing and increased downward turbulent fluxes
- These large eddies alter turbulence structures and cause transitions from a VSBL to a weakly stable boundary layer

Supporting Information:

Supporting Information may be found in the online version of this article.

Correspondence to:

H. Liu,
heping.liu@wsu.edu

Citation:

Lan, C., Liu, H., Katul, G. G., Li, D., & Finn, D. (2022). Turbulence structures in the very stable boundary layer under the influence of wind profile distortion. *Journal of Geophysical Research: Atmospheres*, *127*, e2022JD036565. https://doi.org/10.1029/2022JD036565

Received 27 JAN 2022
Accepted 21 SEP 2022

Author Contributions:

Conceptualization: Heping Liu
Data curation: Gabriel G. Katul, Dan Li, Dennis Finn
Formal analysis: Changxing Lan, Heping Liu
Funding acquisition: Heping Liu, Gabriel G. Katul, Dan Li
Investigation: Changxing Lan, Heping Liu, Gabriel G. Katul, Dan Li
Methodology: Changxing Lan, Heping Liu, Gabriel G. Katul, Dan Li
Project Administration: Heping Liu
Software: Changxing Lan
Supervision: Heping Liu
Validation: Changxing Lan, Heping Liu
Writing – original draft: Changxing Lan, Heping Liu
Writing – review & editing: Heping Liu, Gabriel G. Katul, Dan Li, Dennis Finn

Turbulence Structures in the Very Stable Boundary Layer Under the Influence of Wind Profile Distortion

Changxing Lan[1,2], Heping Liu[1], Gabriel G. Katul[3], Dan Li[4], and Dennis Finn[5]

[1]Department of Civil and Environmental Engineering, Washington State University, Pullman, WA, USA, [2]Institute of Meteorology and Climate Research—Atmospheric Environmental Research, Karlsruhe Institute of Technology, Karlsruhe, Germany, [3]Department of Civil and Environmental Engineering, Duke University, Durham, NC, USA, [4]Department of Earth and Environment, Boston University, Boston, MA, USA, [5]NOAA, Air Resources Laboratory, Idaho Falls, ID, USA

Abstract In very stable boundary layers (VSBL), a "cocktail" of submeso motions routinely result in elevated mean wind speed maxima above the ground, acting as a new source of turbulence generation. This new source of turbulent kinetic energy enhances turbulent mixing and causes mean wind profile distortion (WPD). As a results, this transient distortion in the wind profile adjusts the classical log-law. Addressing how WPD-induced turbulence regulates flow structures, turbulent fluxes, and transitions in stability regimes across layers remains a challenge. Eddy covariance data measured at four levels on a 62-m tower are employed to address these questions. It is shown that the WPD initiates large turbulent eddies that penetrate downward, leading to enhanced vertical mixing and comparable turbulent transport efficiencies across layers. As a consequence, turbulence intensity and fluxes are increased. As the WPD is intensified, turbulent fluxes and turbulent flux transport caused by large eddies are also enhanced, leading to a transition from very stable to weakly stable regimes. Due to the influence of WPD-induced large eddies, the large-eddy turbulent Prandtl number does not deviate appreciably from unity and the partitioning between turbulent kinetic and potential energies is linearly related to the gradient Richardson number.

1. Introduction

Very stable boundary layers (VSBL) at night are commonly characterized by low winds and weak vertical mixing, permitting build-up of air pollutants near the surface and causing air quality concerns (Liu et al., 2020; Tritscher et al., 2020). Additionally, several hazardous weather events such as fog and frost/icing that influence safety (e.g., air and road transportation) and impact agriculture (e.g., nighttime freezing conditions that damage crops) are related to the presence of VSBL. The VSBL remains a "thorny" issue for numerical weather prediction (NWP) models largely because of their reliance on Monin–Obukhov similarity theory (MOST). The VSBL is characterized by weak and intermittent turbulence that does not conform to the assumptions leading to MOST (Liang et al., 2014; Salmond & McKendry, 2005). Furthermore, the suppressed turbulent eddies and the shallow boundary layer could become an exclusively subgrid feature in NWP models. Therefore, a description of the dominant time scale impacting the vertical structures of the mean flow and turbulent statistics as well as the associated turbulent transport and flux exchange remain a subject of active research (Acevedo et al., 2016; Lan et al., 2018; Mahrt, 2008; Mortarini et al., 2018; Sun et al., 2012; Van De Wiel et al., 2007).

In the VSBL where mean wind speeds increase with height z from the ground, turbulent kinetic energy (TKE) is primarily generated by local shear at z, which then acts to energize the horizontal contribution of TKE. However, thermal stratification acts to suppress the vertical contribution of TKE. Moreover, suppressive buoyancy forces can be sufficiently large to result in spatial and temporal intermittent turbulence (Cava et al., 2019). The associated turbulent eddies are often confined to thin layers, causing weak vertical mixing and vertically layered, decoupled stable boundary layer (Lan et al., 2018). As a consequence, turbulent statistics are weakly correlated among different layers in the atmosphere, and vertical gradients in TKE become large in magnitude (Lan et al., 2018). In this regime, sensible heat fluxes often become too small to balance surface radiative cooling (Acevedo et al., 2016; Oldroyd et al., 2014; Van De Wiel et al., 2012) and hence thermal gradients are gradually enhanced by the radiative cooling at the surface, resulting in a more stratified SBL with stronger buoyancy destruction of TKE (Cava et al., 2019). Such feedback may persist until occurrences of externally or internally forced nonstationary disturbances enhance turbulence (Katul et al., 2014; Mahrt, 2008; Mortarini et al., 2018; Sorbjan & Czerwinska, 2013). For example, wind meandering induces directional shear (Mortarini et al., 2019),

drainage current and density current lead to flow acceleration (Sun et al., 2002), and internal gravity wave results in buoyancy oscillations (Sorbjan & Czerwinska, 2013). These disturbances may coexist as a complex mix over some time-averaging interval (e.g., 30 min), challenging the classic concept of the SBL and making the fundamental features of the SBL difficult to represent in turbulence models (Mahrt, 2014).

One common consequence of these disturbances is a nonstationary wind profile distortion (WPD), which triggers a burst of turbulence. The WPD refers to the occurrence of a maximum mean wind speed in the atmospheric surface layer, indicating that the mean velocity profile is not monotonically increasing with height (Mahrt, 2007). Although the exact definition and the cause-and-effect relation about WPD have not been established, the potential mechanisms causing WPD have been proposed in previous studies. For instance, drainage flows can generate WPD even with very gentle topographic slopes (Mahrt, 2017). In addition, wave-like motions can effectively alter wind profile, enhancing both wind speed shear and directional shear (Mahrt et al., 2020). Variations in horizontal pressure gradients related to baroclinic systems also influence wind speed, and thus, impact wind profiles (Mahrt et al., 2014). It was also observed that the occurrence of WPD is transient because the mechanism producing this wind speed maximum is not self-sustaining and must collapse. Previous work on the extreme shallow SBL (of about 3 m) in the Antarctic area demonstrated that systematic and periodic intermittent bursting results from unstable wave growth triggered by a free-shear-generated Kelvin–Helmholtz instability (Petenko et al., 2019; Stefanello et al., 2020; Van Der Linden et al., 2020). Subsequently, momentum is exchanged across layers due to the downward turbulent transport, leading to a vertically coupled SBL.

Although the WPD can exhibit a variety of forms, it is often manifested as a mean wind maximum observed in the lower layers of the VSBL (Cava et al., 2019; Mahrt, 2007, 2008). The occurrence of WPD is accompanied by a positive second derivative in the mean wind profile, leading to an inflectional instability that is conducive to the generation of free shear turbulence at elevated layers instead of the ground (Mahrt, 2007; Nappo, 2002). Since wind shear is the main source of turbulence in the SBL, turbulent eddies are first activated in the elevated layers, forming an "upside-down" structure that transports momentum and heat from higher layers downwards toward the surface (Acevedo et al., 2012). Such intermittently enhanced vertical transport associated with WPD violates the constant-flux assumption and degrades the performance of MOST (Cava et al., 2019; Mahrt, 2008; Mortarini et al., 2018). Despite the already recognized roles of the WPD in turbulence production, how the WPD modifies turbulence structures, turbulent fluxes, and transitions of stability regimes across layers in the VSBL remains a formidable challenge and motivates the work here.

Data collected as part of Project Sagebrush are analyzed to address the study objective. This project aimed to study plume dispersion under a variety of atmospheric stability and wind conditions (Finn et al., 2016). The turbulence data were collected by four eddy covariance (EC) systems on a 62-m tower and are analyzed to (a) investigate how WPD affects the turbulent transport efficiency; (b) determine the scale of turbulent eddies that are predominantly caused by WPD; and (c) examine how WPD-induced large eddies regulate the flux, the transition of the SBL, and the eddy diffusivity.

2. Experimental Site, Data, and Methods

2.1. Site, Instruments, and Data Processing

The field experiment was conducted at the Idaho National Laboratory (INL) site, Idaho (43.59°N; 112.94°W; 1,500 m above mean sea level) (Finn et al., 2016). The terrain surrounding the site is flat. The data collected from 29 September to 9 November 2013 are used here. Velocity and air temperature were measured at 10 Hz by four sonic anemometers (CSAT3, Campbell Scientific, Inc.) mounted at 2, 8, 16, and 60 m on a 62-m tower. The sonic anemometers measured the velocity components (i.e., u, longitudinal; v, lateral; and w vertical velocities) and sonic-derived air temperature (T_s). The details about the site and instruments as well as data post-processing procedures are documented elsewhere (Finn et al., 2015, 2016; Gao et al., 2016; Lan et al., 2018, 2019; Liu et al., 2016). Throughout, the following convention is used: $u' = u - \overline{u}$, $w' = w - \overline{w}$, and $T' = T - \overline{T}$ with primed quantities denoting deviations from the 30-min mean state indicated by the overline.

Briefly, the following post-processing was conducted: (a) physically impossible values and spikes in the raw 10-Hz time series are removed and gaps are filled with linear interpolation; (b) double rotation is performed

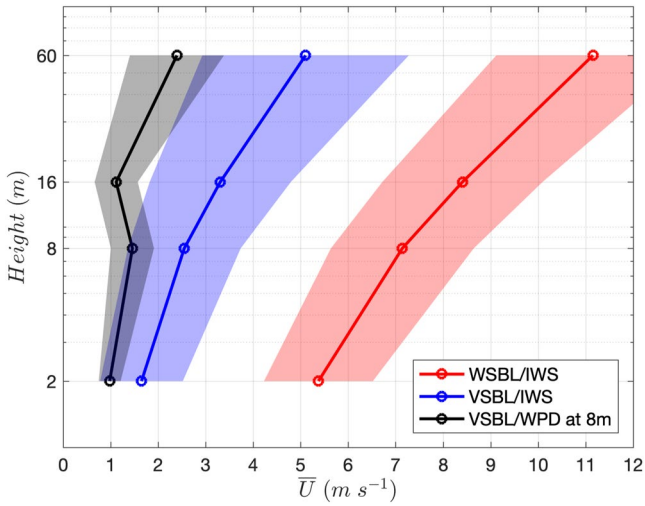

Figure 1. Mean wind speed profiles in the stable boundary layer (SBL). WSBL/IWS: weakly stable boundary layer where wind speeds increase with heights; VSBL/IWS: very stable boundary layer where wind speeds increase with heights; VSBL/WPD: very stable boundary layer with wind profile distortion at 8 m. The shaded areas represent one standard deviation of the averaged wind profiles.

to the sonic anemometer wind velocities; (c) sonic-derived temperature correction and density correction are employed to determine the actual air temperature and air density (Liu et al., 2001; Schotanus et al., 1983; Webb et al., 1980); (d) means, variances, and covariances are calculated with the block average method; and (e) data quality check is then conducted. Specifically, turbulent statistical quantities (e.g., mean, variance, and covariance) are first calculated from coordinate rotated fluctuation time-series using Reynold's averaging over 5-min intervals. These 5-min statistical quantities are then averaged to obtain 30-min means to better represent the SBL statistics over a time scale that is generally used to characterize turbulent fluxes (Lan et al., 2018). For example, to obtain the mean wind profiles, coordinate rotation is performed over 5-min intervals, then the mean wind speed is calculated based on the rotated horizontal wind components (i.e., $\tilde{U} = \sqrt{\tilde{u}^2 + \tilde{v}^2}$, where u is streamwise wind speed and v is lateral wind speed; the tilde is used to indicate 5-min means, the overline is used to represent the 30-min means). The 5-min wind speed is then averaged to obtain 30-min means so that the wind speed can represent the SBL profile over a relatively long period of time and, to some extent, reduce the influence of a sudden increase or decrease in wind speeds. The aggregation of the statistics to 30 min ensures that contributions of internal gravity waves are minimized as demonstrated elsewhere (Sun et al., 2004; Terradellas et al., 2005). To avoid the transition period between daytime and nighttime, only nighttime data from 1900 to 0600 local time are used. Since extremely large values of the local nondimensional stability parameter ($\zeta = z/L$, where L is the Obukhov length) are usually accompanied by negligible sensible heat flux and thus associated with large sampling errors, 30-min segments with ζ greater than 100 are excluded. Consequently, a total of 398 30-min segments is used for the analysis.

2.2. Classification of SBL States

Since one of the main goals is to explore transitions in stability regimes due to WPD, several definitions are introduced. The SBL refers to the stable boundary layer, where the sensible heat flux near the ground is negative. The SBL can be categorized into three distinct regimes based on the relations between $V_{TKE} = \sqrt{\frac{1}{2}\left(\widetilde{u'^2} + \widetilde{v'^2} + \widetilde{w'^2}\right)}$ at the four levels and near-surface wind speed at 2 m (i.e., U_{2m}) as employed in prior studies (Acevedo et al., 2016; Lan et al., 2018; Sun et al., 2012). Using the same data set here, such relations were previously explored in Lan et al. (2018), leading to the following three SBL categories: (a) under weak near-surface winds (i.e., $U_{2m} < 1.6\ m\ s^{-1}$), V_{TKE} increases with height and dV_{TKE}/dz is large, suggesting that the SBL matches a classical "upside-down" representation where the main source of turbulence is elevated and turbulence collapses near the surface due to strong stable stratification; (b) under strong near-surface winds (i.e., $U_{2m} > 4\ m\ s^{-1}$), V_{TKE} become comparable across layers indicating well-mixed conditions (i.e., dV_{TKE}/dz is small); and (c) under moderate near-surface winds (i.e., $1.6\ m\ s^{-1} < U_{2m} < 4\ m\ s^{-1}$), dV_{TKE}/dz is reduced as compared with the case with weak near-surface winds, suggesting that the SBL experiences a transition in stability. The regime III is excluded from the analysis here. Although these thresholds are not universal and may be site-specific, they are surprisingly similar to those found in previous studies (Acevedo et al., 2016; Mortarini et al., 2016; Sun et al., 2012). Consequently, the SBL with U_{2m} less than $1.6\ m\ s^{-1}$ refers to the very stratified and vertically decoupled SBL (VSBL), whereas the SBL with U_{2m} greater than $4\ m\ s^{-1}$ refers to the weakly stratified and vertically coupled SBL (WSBL). Additionally, it can be seen that nonstationarity is the salient feature of the VSBL (Figure S1 in Supporting Information S1).

The average wind profile shows that the mean wind speeds in the WSBL increase with z (labeled as WSBL/IWS in Figure 1 where IWS stands for increased wind speeds, red line). In the VSBL, however, mean wind speeds can either increase with z (labeled as VSBL/IWS in Figure 1, blue line) or show an elevated maximum meaning that

the wind profile experiences a distortion (WPD) (labeled as VSBL/WPD in Figure 1, black line). To quantify the extent of the WPD, each individual wind profile is first normalized by the maximum wind speed occurring at 8 m, followed by calculating the mean (black solid line in Figure S1 in Supporting Information S1) and the three-folds of SD (shaded areas in Figure S1 in Supporting Information S1). The departure of each normalized wind profile from the mean is determined by simply subtracting the mean (red markers in Figure S1 in Supporting Information S1). If the difference is greater than three times of the SD, the case is considered as the VSBL/WPD case (red markers outside the shaded area). The numbers of cases for the three categories are provided in Table S1 in Supporting Information S1. Note that analyzing the WSBL/IWS cases is not the main focus here but only acts as reference for exploring the VSBL (i.e., VSBL/IWS and VSBL/WPD). There are 80 thirty-minute data blocks with WPD occurring at 8 m. The influences of the WPD occurring at 8 m on turbulence structures and fluxes are discussed in the following sections. Since the overall depth of the SBL is shallower than 60 m (Lan et al., 2018), the WPD occurring at 16 m are not considered. Following Mahrt (2007), the second vertical derivative of wind profiles $\left(\text{i.e.,}\frac{\partial^2\overline{U}}{\partial z^2}\right)$ is used to quantify the WPD intensity. To simplify the calculation, the second-order difference is used to approximate the derivative by ignoring the uneven vertical increment $\left(\text{i.e.,}\frac{\Delta^2\overline{U}}{\Delta z^2} \approx \frac{\Delta}{\Delta z_{12-5}}\left(\frac{\Delta\overline{U}}{\Delta z_{16-8}} - \frac{\Delta\overline{U}}{\Delta z_{8-2}}\right)\right)$.

2.3. Definitions of the Single-Level and Cross-Level Wind Direction Change

Single-level wind direction change is defined as the difference in mean wind directions between two consecutive time intervals (i.e., two consecutive 5-min data points). Note that wind direction is calculated as the angle between rotated wind speed (i.e., $\overline{u}$ and $\overline{v}$ are defined as the lateral [easterly] and longitudinal [northerly] winds, respectively). Therefore, the single-level wind direction changes at height z are calculated by

$$\delta_{\mathrm{WD}} = \overline{\mathrm{WD}_{t+1} - \mathrm{WD}_t}, \tag{1}$$

where the subscript t represents time, and the overbar indicates that δ_{WD} is the averaged value of all the 5-min data segments (i.e., 6 runs) in a 30-min segments.

Cross-layer wind direction change is defined as the net change of wind direction between two layers within the same 5-min interval,

$$\Delta_{\mathrm{WD}} = \overline{\mathrm{WD}_{\mathrm{hi}} - \mathrm{WD}_{\mathrm{hj}}}, \tag{2}$$

where subscripts h_i and h_j represent two different layers, and again the overbar represents the averaged Δ_{WD} of all the 5-min data (i.e., six runs) in a 30-min segment. Note that wind directions are first rotated to the range between 0° and 360° to ensure positive values. The maximum δ_{WD} and Δ_{WD} are set to be 180°. For instance, if wind directions change from 320° to 60°, δ_{WD} and Δ_{WD} are determined to be 100°. Equations 1 and 2 are also used elsewhere for the analysis of the same data set (e.g., Finn et al., 2018).

2.4. Ensemble Empirical Mode Decomposition

Ensemble empirical mode decomposition (EEMD) is used without pre-determined functions or treatments to analyze nonstationary and nonlinear turbulence time-series (Huang & Wu, 2008). Compared to traditional low-pass filter based on Fast Fourier Transform, the EEMD has several advantages. Due to the high adaptivity and locality, the EEMD is capable of handling some of the nonlinear and nonstationary occurrences that are ubiquitous in turbulence data for SBL. In addition, the EEMD decomposes the original signal based on a data-driven "sifting process," which extracts signals based on objective frequencies rather than artificial frequency thresholds in the low-pass filter. The EEMD is employed to analyze 30-min time series of turbulent variables. The EEMD decomposes each 30-min time-series into 13 intrinsic mode functions IMF_i (i.e., $i = 1$ to 13) as well as one residual r:

$$x(t) = \sum_{i=1}^{13} \mathrm{IMF}_i(t) + r(t). \tag{3}$$

In the Fourier spectra, each of the components (i.e., IMF_i) shows prominent spectral energy with a distinct corresponding frequency, suggesting that each component represents the signal associated with turbulent eddies with a unique scale. Therefore, the dominant frequency ($\overline{\omega}$) associated with each IMF can be determined by:

$$\overline{\omega}_i = \frac{\int_0^\infty f S_i(f) df}{\int_0^\infty S_i(f) df}, \tag{4}$$

where $S_i(f)$ is the Fourier spectrum of $IMF_i(t)$ (Huang et al., 1998). Additionally, one advantage of the EEMD over other decompositions is that the total covariance calculated from all IMF_i is equivalent to the covariance calculated using the traditional eddy covariance method (i.e., $\overline{w's'_k} = \frac{1}{2}\left(\sum_{i=1}^{14} \overline{IMF_{w',i} IMF_{s',k}} + \sum_{j=1}^{14} \overline{IMF_{w',k} IMF_{s',j}}\right)$, where s represents horizontal wind speed or scalars, and IMF_{14} is the same as the residual mentioned above) (Gao et al., 2017; Lan et al., 2019). Hence, signals of large eddies (or small eddies) can be extracted by summing components with the mean frequencies smaller than (or larger than) a frequency threshold.

3. Results and Discussion

3.1. Wind Profile Distortion and Identification of Large Turbulent Eddies

A conventional quadrant analysis with a hole size of 1 is employed to determine the flux contribution and time fraction associated with sweeps and ejections (Table S2 in Supporting Information S1). It can be seen that the vertical transport of momentum and kinematic heat result largely from sweeps of turbulent eddies, indicative of the significant role of downward penetrating large eddies in transporting momentum and kinematic heat fluxes. How these downward penetrating eddies affect turbulent transport efficiencies of momentum $\left(R_{\mathrm{wu}} = \overline{w'u'}/(\sigma_w \sigma_u)\right)$ and heat ($R_{\mathrm{wT}} = \overline{w'T'}/(\sigma_w \sigma_T)$, where $\sigma_s = \sqrt{\overline{s'^2}}$ is the root-mean squared value of an arbitrary flow variable s) across layers is further investigated (Figure 2). In the WSBL/IWS, turbulent transport efficiencies for momentum flux (and heat flux) at different levels are close to the 1:1 line (blue circles in Figure 2). That means that momentum and heat are transported by the same turbulent eddies across layers with comparable efficiencies. Such transport across layers is performed by the well-developed turbulent eddies with comparable scales, as reflected by the close peak locations in the mid-frequency range of the u, v, and w spectra at 16, 8, and 2 m (Figures 3 and 4a). The vertical mixing induced by these turbulent eddies also contribute to the wu and wT cospectra with comparable magnitudes at the same mid-frequency ranges across layers (Figures 4b and 4c). Note that the global wavelet spectrum proposed by Torrence and Compo (1998) is performed to determine the unbiased and consistent estimation of the true power spectrum for each 30-min segment, and Figures 3 and 4 show the averaged spectra of u, v, and w and the averaged cospectra of wu and wT as a function of dimensionless frequency ($n = fz/\overline{U}$, where $\overline{U}$ is mean wind speed, z is height, and f is natural frequency). The spectral energy density can be interpreted as the contribution of turbulent eddies with different scales to the total variance (or covariance). Totally, there are 106, 80, and 212 30-min segments for WSBL/IWS, VSBL/WPD, and VSBL/IWS, respectively.

In the VSBL/IWS, the large scatter in both R_{wu} and R_{wT} demonstrate that flux transport is performed by turbulent eddies that have different transport efficiencies across layers (black triangles; Figure 2). The u and v spectra in the low-frequency range increase with heights, which is linked to the enhanced influence of submeso motions (Figures 3c and 3d). Such features are similar to those found in previous studies, suggesting that submeso motions are quasi-horizontal, characterized by negligible vertical fluctuations but significantly contribute to horizontal velocity variance of TKE (Acevedo et al., 2016; Mahrt, 2014). Note that the normalized frequencies corresponding to the peaks of the w spectra at 2, 8, and 16 m are close to or larger than 1 (Figure 4d), indicating that the vertical length scale ($L = \overline{U}/f$) of turbulence eddies is less than the observation height, consistent with the results reported by Sun et al. (2012). It also means that large eddies are suppressed and almost detached from the ground (Figure 4d). Due to the vertically suppressed turbulent eddies, it is difficult to observe well-defined cospectral peaks (Figures 4e and 4f).

In the VSBL/WPD, both R_{wu} and R_{wT} become less scattered (red stars; Figure 2), as compared with the VSBL/IWS case. The large values for both the transport efficiencies and R^2 in the VSBL/WPD cases indicate that momentum and heat are transported between layers by turbulent eddies with similar transport efficiencies and such transport is also enhanced, as compared with the VSBL/IWS cases (Table 1). The signs of R_{wu} and R_{wT} are determined

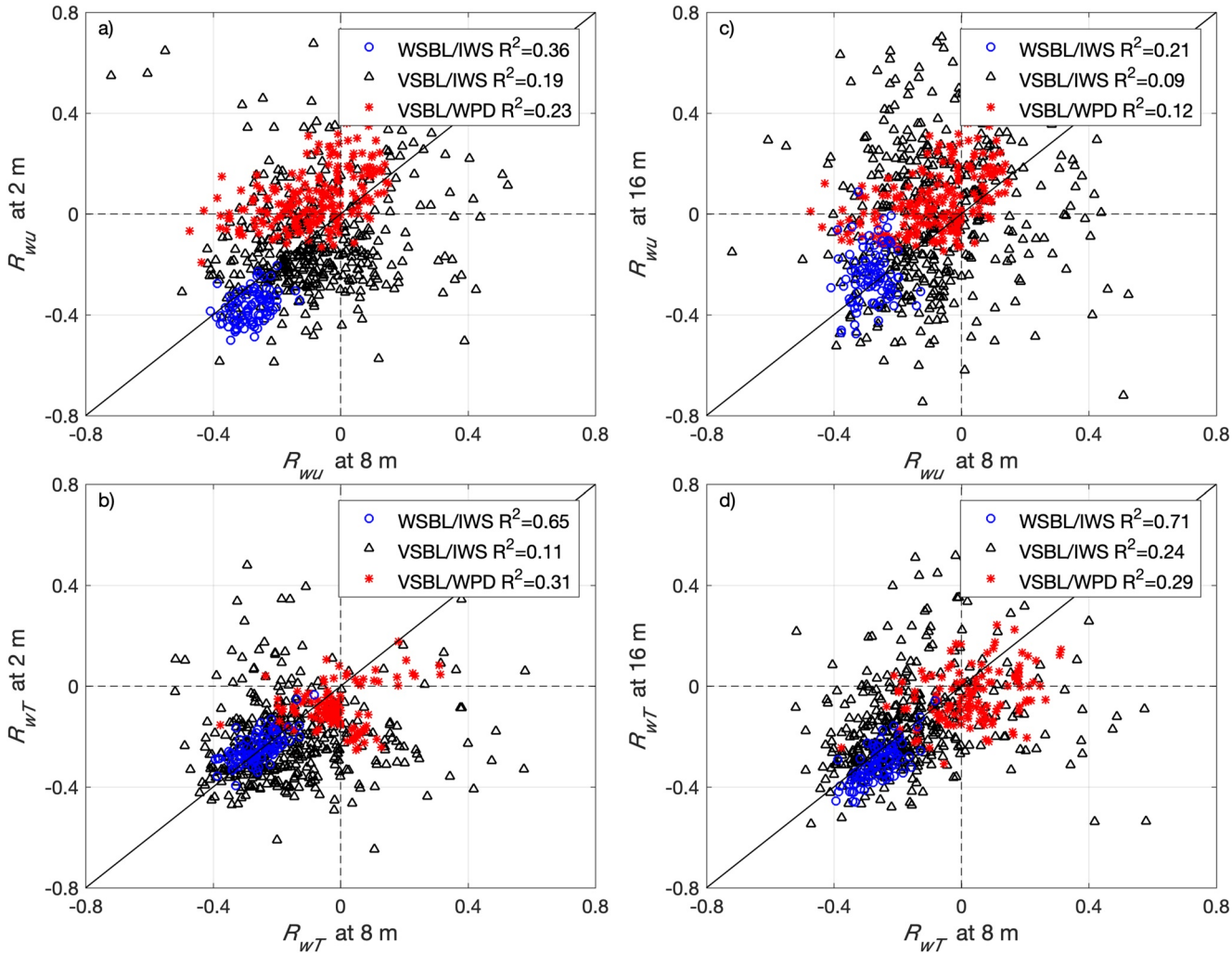

Figure 2. Comparisons of turbulence transport efficiencies for momentum (top panels) and kinematic heat (bottom panels) fluxes between 8 and 2 m (a and b) and between 8 and 16 m (c and d). Blue, green, and red markers represent cases in weakly stable boundary layer where wind speeds increase with heights (WSBL/IWS), very stable boundary layer where wind speeds increase with heights (VSBL/IWS), and very stable boundary layer with wind profile distortion at 8 m (VSBL/WPD).

by the signs of momentum and kinematic heat fluxes, respectively. Therefore, the negative momentum and heat fluxes confirm that the majority of both the momentum and heat is transported downward from 8 m to the surface (Figures 2a and 2b). Although the upward transport of momentum caused by the WPD-induced turbulent eddies is also evident by the positive R_{wu} at 16 m, consistent with the mean wind profile (Figure 2c), heat is primarily transported downward throughout the SBL (Figure 2d). However, the downward penetrating eddies are observed more frequently than the upward moving ones, as reflected by the better agreement of R_{wu} and R_{wT} between 8 and 2 m than those between 8 and 16 m. The significant influence of the WPD on the vertical structure of turbulence is evidenced by the changes in the prominent peaks in the mid-frequency ranges of the w spectra (Figure 4g), even though no obvious changes in their horizontal structures are present (Figures 3e and 3f). The less-than-one normalized frequencies associated with the peaks of the w spectra imply that the WPD-induced turbulent eddies that have comparable scales to the measurement heights interact directly with the surface. Such large eddies enhance momentum and heat transport in the corresponding frequency ranges (Figures 4h and 4i). It is apparent that the significant influence of WPD on vertical turbulence structures primarily occurs at the mid-dimensionless frequency ranges from 0.02 to 0.8, as indicated by the prominent peaks in the w spectra and the wu and wT cospectra; whereas its impact is relatively small at the other scales. Contributions of the WPD-induced, downward penetrating large eddies to momentum and heat fluxes across layers are examined next.

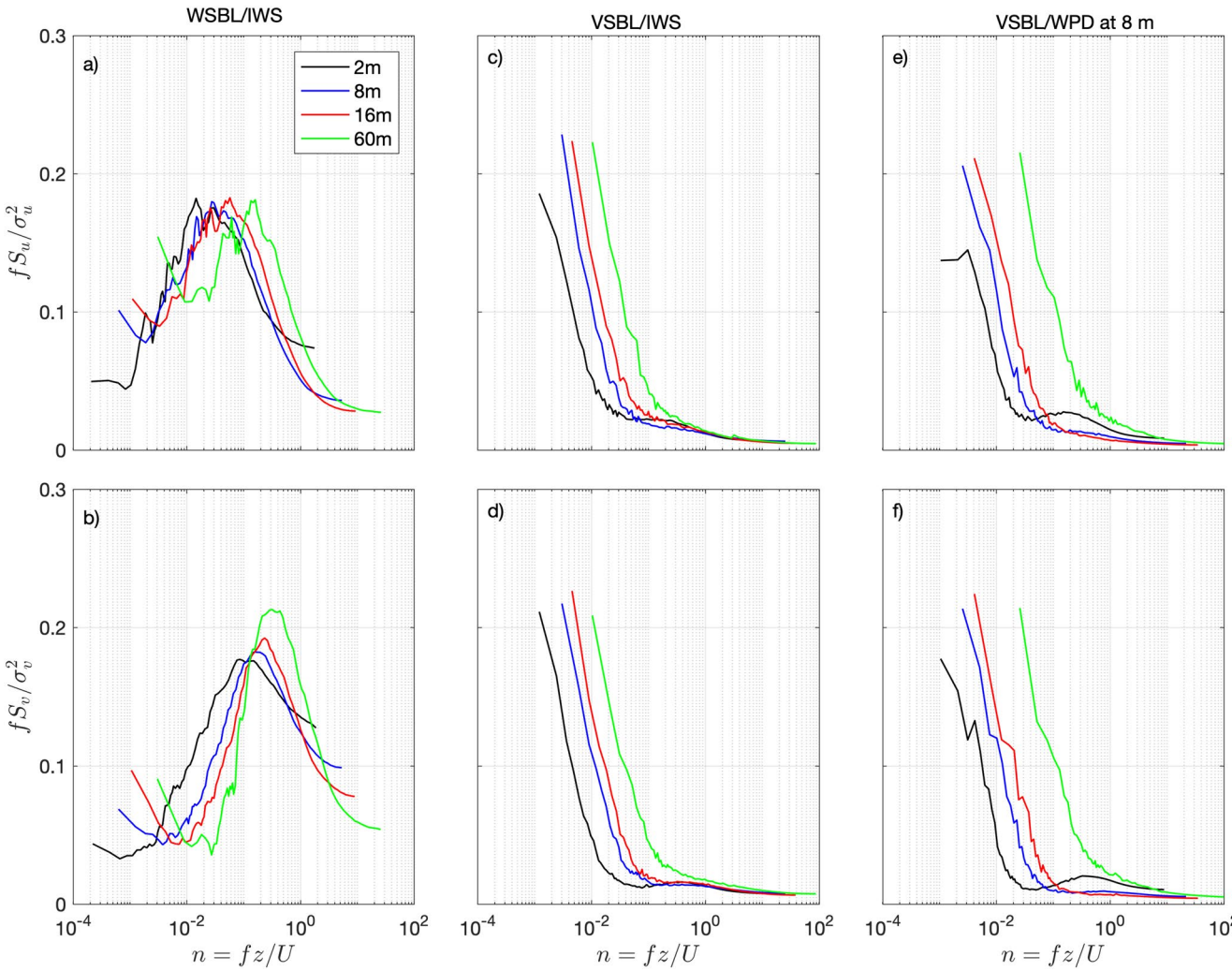

Figure 3. Normalized averaged spectra of u (top panels) and v (bottom panels) as a function of nondimensional frequency ($n = fz/U$, where f is natural frequency, z is height from the ground, and U is mean wind speed). The leftmost to rightmost panels represent weakly stable boundary layer where wind speeds increase with heights (WSBL/IWS, Figure 1, red line); very stable boundary layer where wind speeds increase with heights (VSBL/IWS, Figure 1, blue line), very stable boundary layer with wind profile distortion at 16 m (VSBL/WPD Figure 1, black dash line).

3.2. WPD-Induced Large Eddies Regulate Near Surface Fluxes

To investigate how large eddies affect momentum and heat fluxes, EEMD is now performed to extract large eddies from each 30-min time-series of u', w', and T'. Figure S2 in Supporting Information S1 shows that downward fluxes of momentum and heat are primarily contributed by large eddies that are characterized by the time-series signals from IMF_2 to IMF_7, as reflected by the large relative flux contribution and the corresponding IMF ranges. Therefore, the time-series signals of large eddies are then constructed by summing the time-series signals from IMF_2 to IMF_7 ($x_l = \sum_{i=2}^{7} IMF_i$, subscript l indicates large eddies) for the subsequent analysis. The mean frequency for each IMF is determined by Equation 4 (Table S3 in Supporting Information S1). The results indicate that the frequencies of these oscillatory components (i.e., IMF_2 to IMF_7) range from 0.02 to 0.8, consistent with the observed features in spectra and cospectra discussed in Section 3.1. The contributions to fluxes from horizontal advection (e.g., submeso motions) and background turbulence are reduced by excluding motions with frequencies less than 0.02 (i.e., IMF_1) and larger than 0.8 (IMF_8 to IMF_{13}). It is clear that as the WPD intensity is enhanced, both the downward fluxes of momentum and heat associated with large eddies are increased (Figures 5a and 5b). Moreover, differences in TKE, momentum fluxes, and kinematic heat fluxes between layers

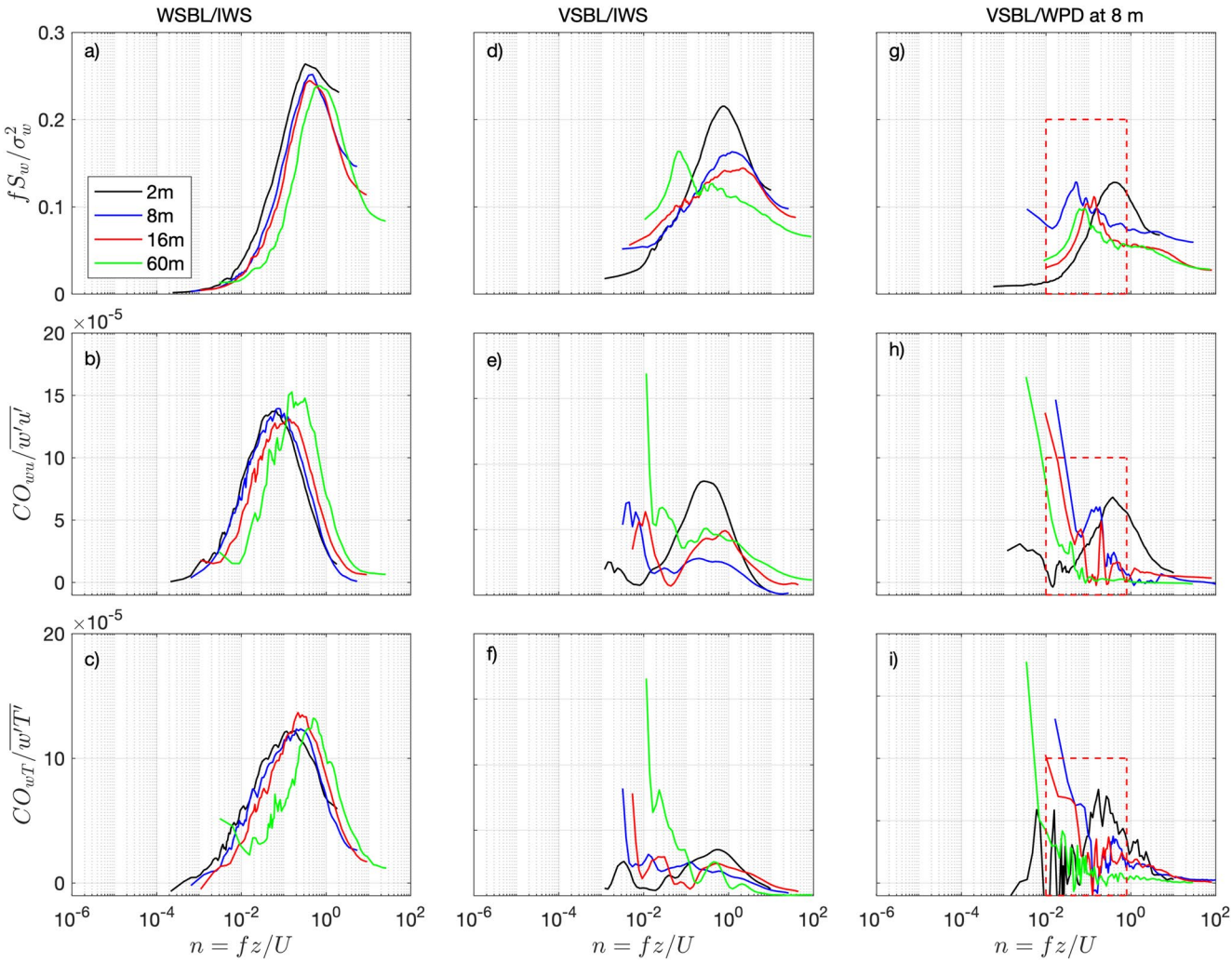

Figure 4. Normalized averaged spectra of w (top panels), and cospectra of wu (middle panels) and wT (bottom panels) as a function of dimensionless frequency ($n = fz/U$, where f is natural frequency, U is mean wind speed, and z is height). The leftmost to rightmost panels represent weakly stable boundary layer where wind speeds increase with heights (WSBL/IWS), very stable boundary layer where wind speeds increase with heights (VSBL/IWS), and very stable boundary layer with wind profile distortion at 8 m (VSBL/WPD).

are largely reduced with the increasing WPD intensity (Figure 5d–5f; see more in Section 3.3). Further, both the turbulent transport efficiencies for momentum $\left(R_{wlul} = \overline{w_l'u_l'}/\left(\sigma_{w_l}\sigma_{u_l}\right)\right)$ and heat $\left(R_{w_lT_l} = \overline{w_l'T_l'}/\left(\sigma_{w_l}\sigma_{T_l}\right)\right)$ fluxes associated with large eddies become less scattered as the WPD intensity increases (Figure 6). Figure 6 also shows that stronger WPD intensities correspond to greater downward transport efficiencies. This feature

Table 1
Mean Values of Turbulent Transport Efficiencies for Momentum and Kinematic Heat Fluxes in the WSBL/IWS, VSBL/IWS, and VSBL/WPD

		2 m	8 m	16 m
WSBL/IWS	R_{wu}	-0.308 ± 0.06	-0.292 ± 0.05	-0.327 ± 0.10
	R_{wT}	-0.152 ± 0.06	-0.174 ± 0.06	-0.189 ± 0.08
VSBL/IWS	R_{wu}	-0.112 ± 0.11	-0.051 ± 0.13	-0.007 ± 0.09
	R_{wT}	-0.022 ± 0.10	-0.003 ± 0.08	-0.007 ± 0.10
VSBL/WPD at 8 m	R_{wu}	-0.0124 ± 0.28	-0.245 ± 0.19	-0.106 ± 0.22
	R_{wT}	-0.097 ± 0.16	-0.085 ± 0.19	-0.041 ± 0.18

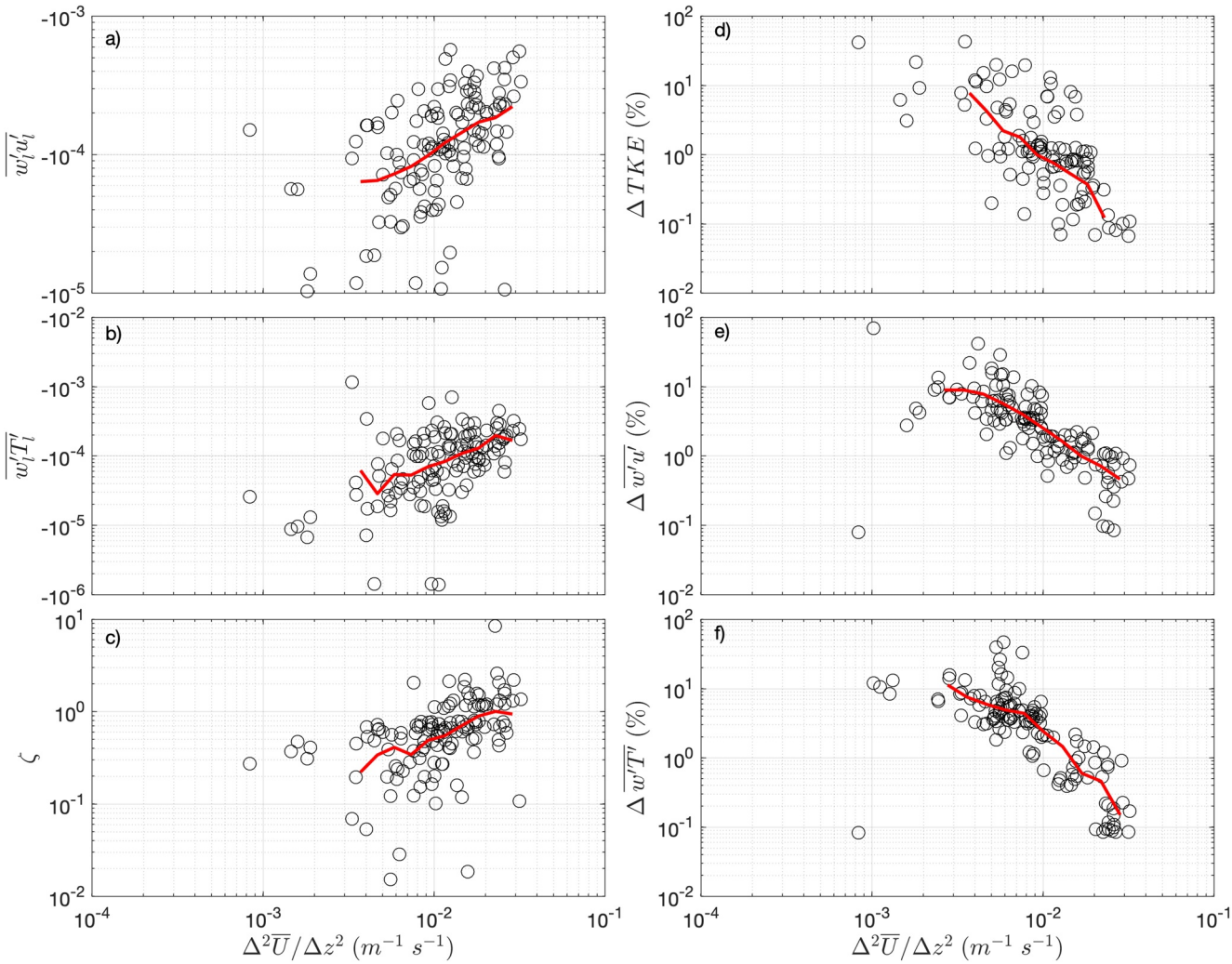

Figure 5. Variations of turbulent fluxes caused by large eddies and stability parameters (left panels) as well as cross-layer differences in turbulence kinetic energy (TKE) and fluxes (right panels) with the intensity of the WPD at 8 m using the data presented in Figure 1 (i.e., the VSBL/WPD case). (a) momentum flux (m^2/s^2); (b) kinematic heat flux (K m/s); (c) local atmospheric stability parameter (z/L, where z is the height and L is the Obukhov length scale) at 8 m. Cross-layer differences in (d) TKE (m^2/s^2), (e) momentum flux (m^2/s^2), and (f) kinematic heat flux (K m/s) between 16 and 2 m. The intensity of the WPD is quantified by the second derivative of the wind profile (i.e., $\frac{\Delta^2\overline{U}}{\Delta z^2} \approx \frac{\overline{u}_{16m} - 2\overline{u}_{8m} + \overline{u}_{2m}}{z_{8m}^2}$). Red lines in (a–f) denote the fitting curves as calculated by the unweighted bin-averaged method. In (d–f) the difference in quantities between layers is defined as $\Delta S = \left|\frac{S_{\text{upper}} - S_{\text{lower}}}{S_{\text{lower}}}\right| \times 100\%$, where S denotes variables including TKE and covariances (i.e., $\overline{u'w'}$, and $\overline{w'\theta'}$).

further confirms that WPD-induced large eddies penetrate downward and transport momentum and heat with comparable efficiencies.

3.3. WPD-Induced Large Eddies Lead to Transitions in the SBL Stability Regimes

Relations between single-level wind direction changes (δ_{WD}) or cross-layer wind direction changes (Δ_{WD}) and U_{2m} are now employed to characterize the SBL (Figure 7). Large δ_{WD} (and Δ_{WD}) occurs in VSBL/IWS that is subjected to the influence of horizontal meandering under weak wind conditions (black circles in Figure 7 under weak winds). Both δ_{WD} and Δ_{WD} decrease with increasing $U_{2\text{m}}$, indicating that wind directions are vertically aligned and the atmospheric surface layer becomes vertically coupled under stronger wind conditions, signaling a transition from VSBL to WSBL (cf., black circles and blue triangles in Figure 7). It is evident that both δ_{WD} and Δ_{WD} are decreased once the WPD occurs (red stars in Figure 7) even though $U_{2\text{m}}$ remains low. This finding confirms that the VSBL becomes vertically coupled as a result of downward penetrating large eddies.

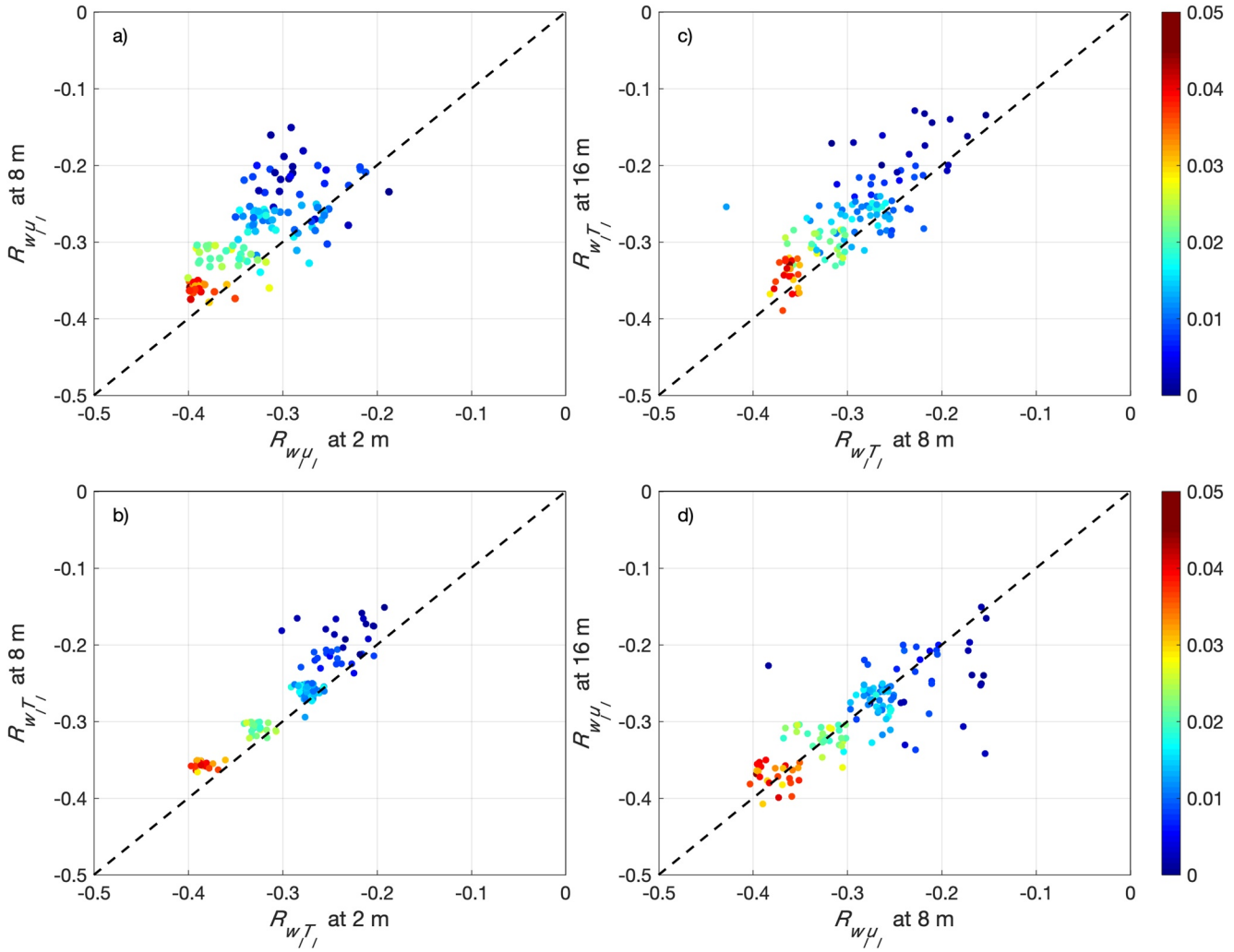

Figure 6. Turbulence transport efficiency for momentum flux (left panels) and kinematic heat flux (right panels) caused by large eddies: comparisons between 8 and 2 m (a and c) and between 8 and 16 m (b and d) when the WPD occurs at 8 m. Different colors represent changes in the intensity of WPD as indicated by the color bars.

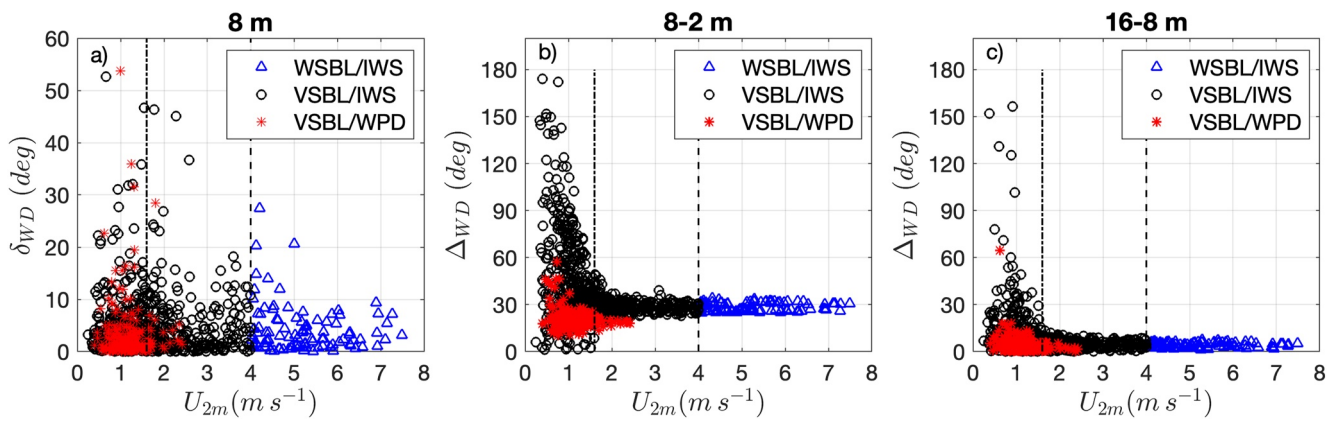

Figure 7. Variations of single-level wind direction change (δ_{WD}) and cross-layer wind direction change (Δ_{WD}) with the near-surface wind speed (U_{2m}). (a) δ_{WD} at 8 m; (b) Δ_{WD} between 8 and 2 m; and (c) Δ_{WD} between 8 and 16 m.

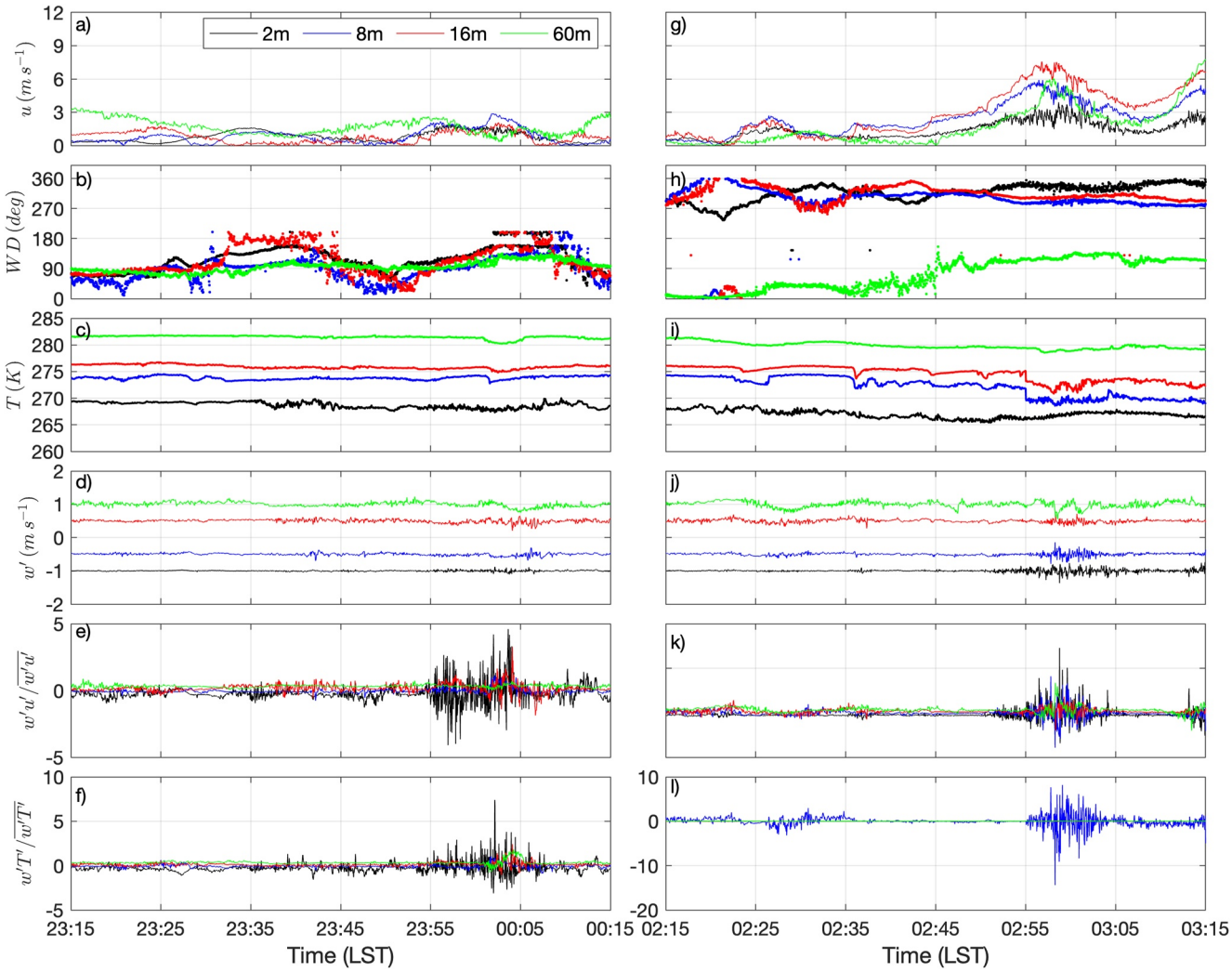

Figure 8. The 1-hr, 10-Hz time series of horizontal mean wind speed (u, a and g), wind direction (WD, b and h), temperature (T, c and i), fluctuation of vertical wind speed (w', d and j), simultaneous normalized momentum flux $\left(w'u'/\overline{w'u'}\right.$, and k), and simultaneous normalized kinematic heat flux ($w'T'/\overline{w'T'}$, f and l) for the VSBL/IWS (23:15–23:45, left panels; 02:15–02:45 right panels) followed by VSBL/WPD (23:55–00:05, left panels; 02:55–03:05 right panels) occurs. The black, red, green, and blue lines denote 2, 8, 16, and 60 m, respectively. Time-series of w', $w'u'$, and $w'T'$ at 8, 16, and 60 m are moved upward for readability. Note that the time used in this study refers to local standard time (i.e., LST).

The influences of WPD on the vertical coupling in the VSBL are also evident from the time-series data shown in Figure 8. In the VSBL/IWS, wind directions not only fluctuate rapidly but also differ largely across levels, showing a vertically decoupled state (e.g., 23:15–23:45 in Figures 8a and 8b; 02:15–02:45 in Figures 8g and 8h) with suppressed turbulent intensity and fluxes (23:15–23:45 in Figures 8c–8f). In the VSBL/WPD (e.g., 23:55–00:05 in Figures 8c–8f; 02:55–03:05 in Figure 8j–8l), wind directions become vertically aligned and more uniform across levels (Figures 8a and 8b) and fluxes become enhanced (Figures 8d–8f). As a consequence, thermal stratifications are weakened (Figure S3 in Supporting Information S1; mean temperature gradients are 4.4 and 2.6 K for the VSBL/IWS and VSBL/WPD cases, respectively) by the enhanced heat transport and vertical mixing, which, in turn, favors further developments of large eddies and their downward penetration (see Figures 4h and 4i). Such weakened stratifications lead to enhanced vertical coupling, even though U_{2m} remains low.

3.4. Influence of Large Eddies on Eddy Diffusivity

The parameterization for turbulence in stable conditions is essential for improving weather, climate, and air quality models. Here, the influence of WPD-induced large eddies on the applicability of K-theory, which is one

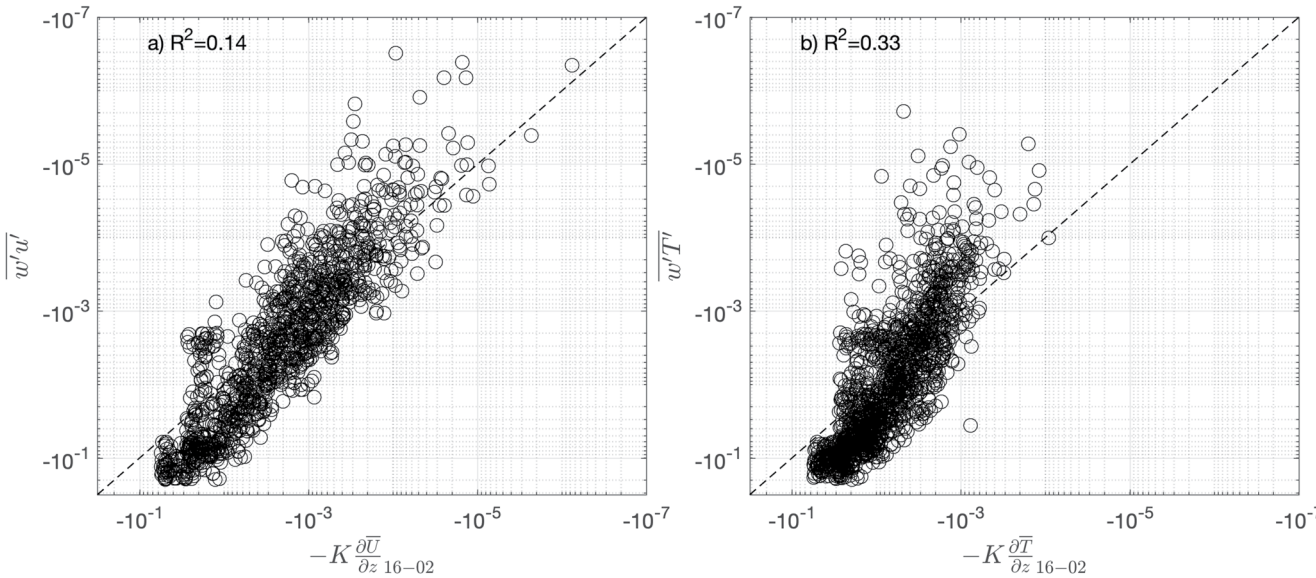

Figure 9. Comparisons (a) between K-theory modeled and measured momentum fluxes (m^2/s^2) and (b) between K-theory modeled and measured kinematic heat fluxes (K m/s) when the WPD occurs at 8 m.

of the cornerstones for turbulence parameterization, is analyzed. The K-theory assumes that turbulent flux of a flow variable A is given by $F = -K\frac{\partial A}{\partial z}$, where K is the vertical eddy diffusivity coefficient here associated with characteristic eddies, F is large-scale turbulent flux (i.e., $\overline{w_l'u_l'}$, and $\overline{w_l'T_l'}$, determined by IMF_2 to IMF_7), and $\frac{\partial A}{\partial z}$ is the mean vertical gradient for a flow variable A (i.e., U or T). Here, K-theory is applied only to the fluxes produced by large-scale eddies with $K = 2\sigma_{w_l}^2\tau_l$, where $\sigma_{w_l}^2$ is vertical turbulent kinetic energy contributed by large eddies only and τ_l is the associated time scale of large eddies determined from the dimensionless frequency of the peak in the vertical velocity spectrum. Figure 9 shows the comparison between modeled momentum and kinematic fluxes by such a K-theory representation and measured fluxes (produced by large scales) when the WPD occurs at 8 m. One prominent feature of Figure 9 is that data points converge to the one-to-one line, which suggests that momentum and kinematic heat fluxes can be approximated by the proposed K-theory for large eddies when formulated from vertical velocity statistics alone. Thus, the eddy diffusivity for large eddies is assumed to be the same for momentum and kinematic heat fluxes ($K_m = K_H = 2\sigma_{w_l}^2\tau_l$). This finding agrees with the data that the inverse Prandtl number is near unity when WPD occurs ($Pr = \frac{K_H}{K_m} = 1$; Businger et al., 1971; Wieringa, 1980).

The consequences of the similarity between momentum and heat fluxes that are transported by large eddies are further analyzed. Similar to the correlation Prandtl number proposed by Mahrt (1991), the K-theory model is employed to parameterize momentum and kinematic heat fluxes, yielding:

$$\frac{R_{w_lT_l}}{R_{w_lu_l}} = \frac{\sigma_{u_l}}{\sigma_{T_l}}\frac{\partial \overline{T}/\partial z}{\partial \overline{U}/\partial z}. \quad (5)$$

Figure 10 shows the comparison of transport efficiencies between momentum and kinematic heat fluxes. For the VSBL/IWS cases, turbulence is largely suppressed by thermal stratification, leading to the weak transport of both momentum and heat (black markers). For the WSBL/IWS cases, momentum and heat are relatively well-mixed due to the enhanced turbulence. The magnitudes of downward heat fluxes are low due to small temperature gradients despite the strong mechanically generated turbulence, leading to the decreased temperature gradient, and thus smaller values of the ratio of $R_{w_lT_l}$ and $R_{w_lu_l}$ (blue markers). In addition, the largest R^2 for the WSBL/IWS cases suggests that momentum and kinematic heat transport become more correlated, implying the enhancement of transport similarity between momentum and heat. Figure 9 indicates that the eddy diffusivity for both momentum and kinematic heat by large eddies can be parameterized by the same equation (i.e., $K_m = K_H = 2\sigma_{w_l}^2\tau_l$). Therefore, the linkage between the observed strong turbulent transport similarity in WSBL/IWS and the near-constant

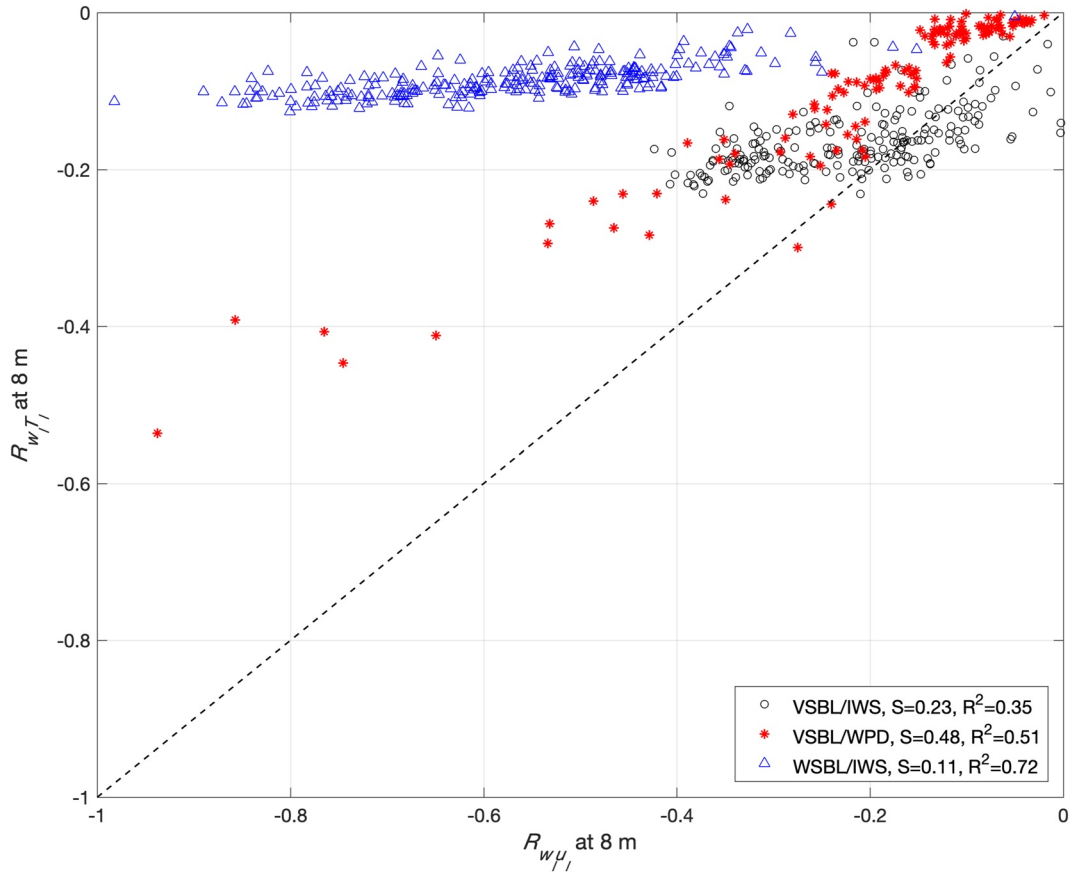

Figure 10. Comparison between turbulent transport efficiencies of momentum and those kinematic heat fluxes measured at 8 m. Turbulent transport efficiencies of momentum and heat are determined as $R_{w_l u_l} = \frac{\overline{w_l' u_l'}}{\sigma_{w_l}\sigma_{u_l}}$ and $R_{w_l T_l} = \frac{\overline{w_l' T_l'}}{\sigma_{w_l}\sigma_{T_l}}$, where the subscript "$l$" denotes large eddies. The slope of the linear regression (S) and the coefficient of determination (R^2) are also provided.

inverse turbulent Prandtl number can be established. This finding is consistent with results in Katul et al. (2014), suggesting that the inverse turbulent Prandtl number ($Pr^{-1} = K_H/K_m$) does not change substantially in weakly stable conditions. The ratio of $R_{w_l T_l}$ and $R_{w_l u_l}$ tends to be a constant ($\frac{R_{w_l T_l}}{R_{w_l u_l}} = S$, where $S \approx 0.48$ as demonstrated in Figure 10, red makers), indicative of a relation between velocity and temperature gradients given as $\frac{\sigma_{u_l}}{\sigma_{T_l}} = S\frac{\partial \overline{U}/\partial z}{\partial \overline{T}/\partial z}$. The broader implications of this outcome are the following. The large-scale $\mathrm{TKE}_l = 0.5\left(\sigma_{u_l}^2 + \sigma_{v_l}^2 + \sigma_{w_l}^2\right) \approx \sigma_{u_l}^2$ (in Figures 3 and 4, the normalized spectra energy of u and v are comparable and much larger than the spectra energy of w) while the large-scale turbulent potential energy $\mathrm{TPE}_l = 0.5\left(g/\overline{T}\right)\sigma_{T_l}^2/\left(\partial \overline{T}/\partial z\right)$, where g is the gravitational acceleration. With these definitions, it directly follows that

$$\frac{\mathrm{TPE}_l}{\mathrm{TKE}_I} = \frac{1}{2S^2} Ri_g, \tag{6}$$

where $Ri_g = (g/T)\left(\partial \overline{T}/\partial z\right)/\left(\partial \overline{U}/\partial z\right)^2$ is the gradient Richardson number set by the mean flow. Virtually all models predict a sublinear increase in TPE/TKE with increasing Ri_g when all scales are considered (Li et al., 2016). The work here goes further to show that the leading effect is a near constant S set by the large scales. Thus, it may be surmised that the partitioning of total turbulent energy (TPE + TKE) into kinetic and potential energy at the large scale appears to be dictated by Ri_g set by the mean flow.

4. Conclusions

Data measured by four EC systems on a 62-m tower are used to examine the role of nonstationary wind profile distortion (labeled as WPD) in regulating turbulence structures and fluxes in the very stable boundary layer (labeled as VSBL) over a flat terrain. WPD is detected by the occurrence of a wind speed maximum at 8 m. WPD initiates large turbulent eddies with dimensionless frequencies from 0.02 to 0.8. These WPD-induced large eddies with vertical scales comparable to their observation heights penetrate downward, acting as well-organized structures appearing across layers (vertical velocity spectra peaking at those frequencies). As a consequence, such large eddies lead to vertically aligned wind directions, enhanced turbulent transport efficiencies, increased fluxes, and reduced across-layer TKE and flux differences. Further, WPD-induced large eddies play a significant role in regulating transitions from VSBL to WSBL with enhanced vertical mixing and coupling across layers. The work here supports similarity in effective large-scale eddy diffusivities for momentum and heat given by $K_m = K_H = 2\sigma_{w_l}^2 \tau_l$, where $\sigma_{w_l}^2$ is the variance of the large-scale vertical velocity and τ_l is inferred from the dimensionless frequency of the large-scale vertical velocity. The similarity between momentum and heat diffusivities at large scales implies that the partitioning between large-scale turbulent kinetic and potential energies is linearly related to the mean gradient Richardson number. This gradient Richardson number is primarily set by the mean flow, which is further affected by radiative cooling at the ground and mean wind speed maxima during the WPD.

Data Availability Statement

The data used in this paper are deposited in a public repository (https://zenodo.org/record/7187717#.Y0ZTyC8Rr0o). Dataset citation: Lan et al. (2022). Turbulence structures in the very stable boundary layer under the influence of wind profile distortion https://doi.org/10.5281/zenodo.7187717.

Acknowledgments
The authors thank S. Beard, T. Strong, B. Reese, E. Russell, and Z. Gao for their assistance in the field experiment and two anonymous reviewers are acknowledged for their constructive comments and numerous suggestions. Heping Liu, Gabriel G. Katul, and Dan Li acknowledge support from the U.S. National Science Foundation (NSF-AGS-1419614, NSF-AGS-1853050, NSF-AGS-1644382, NSF-AGS-1853354, and NSF-AGS-2028633). Gabriel G. Katul also acknowledges partial support from the U.S. Department of Energy (DE-SC0022072). Changxing Lan thanks the China Scholarship Council (CSC) for additional support.

References

Acevedo, O. C., Costa, F. D., & Degrazia, G. A. (2012). The coupling state of an idealized stable boundary layer. *Boundary-Layer Meteorology*, *145*(1), 211–228. https://doi.org/10.1007/s10546-011-9676-3

Acevedo, O. C., Mahrt, L., Puhales, F. S., Costa, F. D., Medeiros, L. E., & Degrazia, G. A. (2016). Contrasting structures between the decoupled and coupled states of the stable boundary layer. *Quarterly Journal of the Royal Meteorological Society*, *142*(695), 693–702. https://doi.org/10.1002/qj.2693

Businger, J. A., Wyngaard, J. C., Izumi, Y., & Bradley, E. F. (1971). Flux-profile relationships in the atmospheric surface layer. *Journal of the Atmospheric Sciences*, *28*(2), 181–189. https://doi.org/10.1175/1520-0469(1971)028<0181:fprita>2.0.co;2

Cava, D., Mortarini, L., Giostra, U., Acevedo, O., & Katul, G. (2019). Submeso motions and intermittent turbulence across a nocturnal low-level jet: A self-organized criticality analogy. *Boundary-Layer Meteorology*, *172*, 17–43. https://doi.org/10.1007/s10546-019-00441-8

Finn, D., Clawson, K. L., Eckman, R. M., Carter, R. G., Rich, J. D., Strong, T. W., et al. (2015). *Project Sagebrush Phase 1, NOAA Technical Memorandum OAR ARL-268*, Air Resources Laboratory. 338. https://doi.org/10.7289/V5VX0DHV

Finn, D., Eckman, R., Gao, Z., & Liu, H. (2018). Mechanisms for wind direction changes in the very stable boundary layer. *Journal of Applied Meteorology*, *57*, 2623–2637. https://doi.org/10.1175/JAMC-D-18-0065.1

Finn, D., Reese, B., Butler, B., Wagenbrenner, N., Clawson, K. L., Rich, J., et al. (2016). Evidence for gap flows in the Birch Creek Valley, Idaho. *Journal of the Atmospheric Sciences*, *73*(12), 4873–4894. https://doi.org/10.1175/JAS-D-16-0052.1

Gao, Z., Liu, H., Katul, G. G., & Foken, T. (2017). Non-closure of the surface energy balance explained by phase difference between vertical velocity and scalars of large atmospheric eddies. *Environmental Research Letters*, *12*(3), 034025. https://doi.org/10.1088/1748-9326/aa625b

Gao, Z., Liu, H., Russell, E. S., Huang, J., Foken, T., & Oncley, S. P. (2016). Large eddies modulating flux convergence and divergence in a disturbed unstable atmospheric surface layer. *Journal of Geophysical Research: Atmospheres*, *121*, 1475–1492. https://doi.org/10.1002/2015JD024529

Huang, N. E., Shen, Z., Long, S. R., Wu, M. C., Shih, H. H., Zheng, Q., et al. (1998). The empirical mode decomposition and the Hilbert spectrum for nonlinear and non-stationary time series analysis. *Proceedings of the Royal Society A*, *454*(1971), 903–995. https://doi.org/10.1098/rspa.1998.0193

Huang, N. E., & Wu, Z. (2008). A review on Hilbert-Huang transform: Method and its applications to geophysical studies. *Reviews of Geophysics*, *46*(2). https://doi.org/10.1029/2007RG000228

Katul, G. G., Porporato, A., Shah, S., & Bou-Zeid, E. (2014). Two phenomenological constants explain similarity laws in stably stratified turbulence. *Physical Review E*, *89*(2), 023007. https://doi.org/10.1103/PhysRevE.89.023007

Lan, C., Liu, H., Katul, G. G., Li, D., & Finn, D. (2019). Large eddies regulate turbulent flux gradients in coupled stable boundary layers. *Geophysical Research Letters*, *46*, 6090–6100. https://doi.org/10.1029/2019GL082228

Lan, C., Liu, H., Katul, G. G., Li, D., & Finn, D. (2022). Turbulence structures in the very stable boundary layer under the influence of wind profile distortion [Dataset]. Zenodo, https://doi.org/10.5281/zenodo.5899660

Lan, C., Liu, H., Li, D., Katul, G. G., & Finn, D. (2018). Distinct turbulence structures in stably stratified boundary layers with weak and strong surface shear. *Journal of Geophysical Research: Atmospheres*, *123*, 7839–7854. https://doi.org/10.1029/2018JD028628

Li, D., Katul, G. G., & Zilitinkevich, S. S. (2016). Closure schemes for stably stratified atmospheric flows without turbulence cutoff. *Journal of the Atmospheric Sciences*, *73*, 4817–4832. https://doi.org/10.1175/JAS-D-16-0101.1

Liang, J., Zhang, L., Wang, Y., Cao, X., Zhang, Q., Wang, H., & Zhang, B. (2014). Turbulence regimes and the validity of similarity theory in the stable boundary layer over complex terrain of the Loess Plateau, China. *Journal of Geophysical Research: Atmospheres*, *119*, 6009–6021. https://doi.org/10.1002/2014JD021510

Linden, S., Wiel, B., Petenko, I., Heerwaarden, C., Jonker, H., & Jonker, H. J. J. (2020). A businger mechanism for intermittent bursting in the stable boundary layer. *Journal of the Atmospheric Sciences*, *77*(10), 1–3360. https://doi.org/10.1175/JAS-D-19-0309.1

Liu, C., Huang, J., Wang, Y., Tao, X., Hu, C., Deng, L., et al. (2020). Vertical distribution of PM2.5 and interactions with the atmospheric boundary layer during the development stage of a heavy haze pollution event. *Science of the Total Environment*, *704*, 704. https://doi.org/10.1016/j.scitotenv.2019.135329

Liu, H., Peters, G., & Foken, T. (2001). New equations for sonic temperature variance and buoyancy heat flux with an omnidirectional sonic anemometer. *Boundary-Layer Meteorology*, *100*(3), 459–468. https://doi.org/10.1023/A:1019207031397

Liu, H., Zhang, Q., Katul, G. G., Cole, J. J., Chapin, F. S., III, & MacIntyre, S. (2016). Large CO2 effluxes at night and during synoptic weather events significantly contribute to CO2 emissions from a reservoir. *Environmental Research Letters*, *11*(6), 64001. https://doi.org/10.1088/1748-9326/11/6/064001check doi

Mahrt, L. (1991). Eddy asymmetry in the sheared heated boundary layer. *Journal of the Atmospheric Sciences*, *48*(3), 472–492. https://doi.org/10.1175/1520-0469(1991)048<0472:eaitsh>2.0.co;2

Mahrt, L. (2007). Weak-wind mesoscale meandering in the nocturnal boundary layer. *Environmental Fluid Mechanics*, *7*, 331–347. https://doi.org/10.1007/s10652-007-9024-9

Mahrt, L. (2008). The influence of transient flow distortion on turbulence in stable weak-wind conditions. *Boundary-Layer Meteorology*, *127*, 1–16. https://doi.org/10.1007/s10546-007-9244-z

Mahrt, L. (2014). Stably stratified atmospheric boundary layers. *Annual Review of Fluid Mechanics*, *46*(1), 23–45. https://doi.org/10.1146/annurev-fluid-010313-141354

Mahrt, L. (2017). Stably stratified flow in a shallow valley. *Boundary-Layer Meteorology*, *162*(1), 1–20. https://doi.org/10.1007/s10546-016-0191-4

Mahrt, L., Pfister, L., & Thomas, C. K. (2020). Small-scale variability in the nocturnal boundary layer. *Boundary-Layer Meteorology*, *174*(1), 81–98. https://doi.org/10.1007/s10546-019-00476-x

Mahrt, L., Richardson, S., Stauffer, D., & Seaman, N. (2014). Nocturnal wind-directional shear in complex terrain. *Quarterly Journal of the Royal Meteorological Society*, *140*(685), 2393–2400. https://doi.org/10.1002/qj.2369

Mortarini, L., Cava, D., Giostra, U., Acevedo, O., Nogueira Martins, L., Soares de Oliveira, P. E., & Anfossi, D. (2018). Observations of submeso motions and intermittent turbulent mixing across a low level jet with a 132-m tower. *Quarterly Journal of the Royal Meteorological Society*, *144*, 172–183. https://doi.org/10.1002/qj.3192

Mortarini, L., Cava, D., Giostra, U., Costa, F. D., Degrazia, G., Anfossi, D., & Acevedo, O. (2019). Horizontal meandering as a distinctive feature of the stable boundary layer. *Journal of the Atmospheric Sciences*, *76*(10), 3029–3046. https://doi.org/10.1175/JAS-D-18-0280.1

Mortarini, L., Stefanello, M., Degrazia, G., Roberti, D., Trini Castelli, S., & Anfossi, D. (2016). Characterization of wind meandering in low-wind- speed conditions. *Boundary-Layer Meteorology*, *161*(1), 165–182. https://doi.org/10.1007/s10546-016-0165-6

Nappo, C. J. (2002). *An introduction to atmospheric gravity waves* (p. 297). Academic Press.

Oldroyd, H. J., Katul, G., Pardyjak, E. R., & Parlange, M. B. (2014). Momentum balance of katabatic flow on steep slopes covered with short vegetation. *Geophysical Research Letters*, *41*(13), 4761–4768. https://doi.org/10.1002/2014GL060313

Petenko, I., Argentini, S., Casasanta, G., Genthon, C., & Kallistratova, M. (2019). Stable surface-based turbulent layer during the polar winter at Dome C, Antarctica: Sodar and in situ observations. *Boundary-Layer Meteorology*, *171*, 101–128. https://doi.org/10.1007/s10546-018-0419-6

Salmond, J. A., & McKendry, I. G. (2005). A review of turbulence in the very stable nocturnal boundary layer and its implications for air quality. *Progress in Physical Geography*, *29*, 171–188. https://doi.org/10.1191/0309133305pp442ra

Schotanus, P., Nieuwstadt, F. T. M., & De Bruin, H. A. R. (1983). Temperature measurement with a sonic anemometer and its application to heat and moisture fluxes. *Boundary-Layer Meteorology*, *26*(1), 81–93. https://doi.org/10.1007/BF00164332

Sorbjan, Z., & Czerwinska, A. (2013). Statistics of turbulence in the stable boundary layer affected by gravity waves. *Boundary-Layer Meteorology*, *148*(1), 73–91. https://doi.org/10.1007/s10546-013-9809-y

Stefanello, M., Cava, D., Giostra, U., Acevedo, O., Degrazia, G., Anfossi, D., & Mortarini, L. (2020). Influence of submeso motions on scalar oscillations and surface energy balance. *Quarterly Journal of the Royal Meteorological Society*, *146*, 889–903. https://doi.org/10.1002/qj.3714

Sun, J., Burns, S. P., Lenschow, D. H., Banta, R., Newsom, R., Coulter, R., et al. (2002). Intermittent turbulence associated with a density current passage in the stable boundary layer. *Boundary-Layer Meteorology*, *105*, 199–219. https://doi.org/10.1023/A:1019969131774

Sun, J., Lenschow, D. H., Burns, S. P., Banta, R. M., Newsom, R. K., Coulter, R., et al. (2004). Atmospheric disturbances that generate intermittent turbulence in nocturnal boundary layers. *Boundary-Layer Meteorology*, *110*(2), 255–279. https://doi.org/10.1023/A:1026097926169

Sun, J., Mahrt, L., Banta, L. M., & Pichugina, Y. L. (2012). Turbulence regimes and turbulence intermittency in the stable boundary layer during CASES-99. *Journal of the Atmospheric Sciences*, *69*(1), 338–351. https://doi.org/10.1175/JAS-D-11-082.1

Terradellas, E., Soler, M. R., Ferreres, E., & Bravo, M. (2005). Analysis of oscillations in the stable atmospheric boundary layer using wavelet methods. *Boundary-Layer Meteorology*, *114*(3), 489–518. https://doi.org/10.1007/s10546-004-1293-y

Torrence, C., & Compo, G. P. (1998). A practical guide to wavelet analysis. *Bulletin of the American Meteorological society*, *79*(1), 61–78. https://doi.org/10.1175/1520-0477(1998)079⟨0061:APGTWA⟩2.0.CO;2

Tritscher, T., Raz, R., Levi, Y., Levy, I., Broday, D. M., & Broday, D. M. (2020). Emissions vs. turbulence and atmospheric stability: A study of their relative importance in determining air pollutant concentrations. *Science of the Total Environment*, *733*, 733. https://doi.org/10.1016/j.scitotenv.2020.139300

Van Der Linden, S. J., Van De Wiel, B. J., Petenko, I., Van Heerwaarden, C. C., Baas, P., & Jonker, H. J. (2020). A Businger mechanism for intermittent bursting in the stable boundary layer. *Journal of the Atmospheric Sciences*, *77*(10), 3343–3360. https://doi.org/10.1175/JAS-D-19-0309.1

Van De Wiel, B. J. H., Moene, A. F., Jonker, H. J. J., Baas, P., Basu, S., Donda, J. M. M., et al. (2012). The minimum wind speed for sustainable turbulence in the nocturnal boundary layer. *Journal of the Atmospheric Sciences*, *69*, 3116–3127. https://doi.org/10.1175/JAS-D-12-0107.1

Van De Wiel, B. J. H., Moene, A. F., Steeneveld, G. J., Hartogensis, O. K., & Holtslag, A. A. M. (2007). Predicting the collapse of turbulence in stably stratified boundary layers. *Flow, Turbulence and Combustion*, *79*(3), 251–274. https://doi.org/10.1007/s10494-007-9094-2

Webb, E. K., Pearman, G. I., & Leuning, R. (1980). Correction of flux measurements for density effects due to heat and water vapour transfer. *Quarterly Journal of the Royal Meteorological Society*, *106*(447), 85–100. https://doi.org/10.1002/qj.49710644707

Wieringa, J. (1980). A revaluation of the Kansas mast influence on measurements of stress and cup anemometer overspeeding. *Boundary-Layer Meteorology*, *18*, 411–430. https://doi.org/10.1007/BF00119497